






# Terahertz Metamaterial Optoelectronic Modulators With GHz Reconfiguration Speed

Abdullah M. Zaman , Graduate Student Member, IEEE, Yuezhen Lu , Xavier Romain, Nikita W. Almond, Oliver J. Burton , Jack Alexander-Webber, Stephan Hofmann, Thomas Mitchell , Jonathan D. P. Griffiths, Harvey E. Beere, David A. Ritchie, and Riccardo Degl'Innocenti 

**Abstract**—All-electronic ultrafast control of terahertz radiation is demonstrated in integrated metamaterial/graphene devices. By electrostatic gating the graphene conductivity, the overall optical response of the incident terahertz  $E$ -field is modified. Depending on the configuration, amplitude, phase, and polarization of terahertz radiation could be modulated with GHz range of reconfiguration speed. An extinction ratio of  $>7.6$  dB in amplitude is achieved at the resonant frequency of 0.75 THz. Additionally, a relative phase shift of  $>17.4^\circ$  is observed around a frequency of 0.68 THz. When operating as a polarization modulator, the device has reported an ellipticity change of  $\sim 40\%$  at a frequency of 0.68 THz and a dynamic rotation of the polarization plane by  $>9^\circ$  at resonance. The switching capability of the modulators has been investigated all electronically reporting a speed exceeding 3 GHz, only limited by the available instrumentation. Consequently, GHz-speed of modulation can be achieved for frequencies around 0.75 THz. These results represent a breakthrough for all applications where a fast, versatile, and efficient modulation of THz radiation is required, such as in next-generation wireless communication, quantum electronics, and ultrafast imaging.

**Index Terms**—Graphene, integrated modulators, metamaterials (MMs), terahertz (THz), wireless communications.

## I. INTRODUCTION

RESEARCH in optoelectronics integrated devices, such as modulators and detectors, operating in the terahertz (THz)

Manuscript received 4 March 2022; revised 4 May 2022; accepted 13 May 2022. Date of publication 30 May 2022; date of current version 3 September 2022. The work of Abdullah M. Zaman, Yuezhen Lu, Xavier Romain, and Riccardo Degl'Innocenti was supported by Engineering and Physical Sciences Research Council under Grant EP/S019383/1. (Corresponding author: Abdullah M. Zaman.)

Abdullah M. Zaman is with the Department of Engineering, University of Lancaster, Lancaster LA1 4YW, U.K., and also with the College of Engineering, Taibah University, Madina 42353, Saudi Arabia (e-mail: abdozaman99@yahoo.com).

Yuezhen Lu, Xavier Romain, and Riccardo Degl'Innocenti are with the Department of Engineering, University of Lancaster, Lancaster LA1 4YW, U.K. (e-mail: y.lu39@lancaster.ac.uk; x.romain@lancaster.ac.uk; r.deglinnocenti@lancaster.ac.uk).

Nikita W. Almond, Thomas Mitchell, Jonathan D. P. Griffiths, Harvey E. Beere, and David A. Ritchie are with Cavendish Laboratory, University of Cambridge, Cambridge CB3 0HE, U.K. (e-mail: na470@cam.ac.uk; tam46@cam.ac.uk; jpg35@cam.ac.uk; heb1000@cam.ac.uk; dar11@cam.ac.uk).

Oliver J. Burton, Jack Alexander-Webber, and Stephan Hofmann are with the Department of Engineering, University of Cambridge, Cambridge CB3 0FA, U.K. (e-mail: ob303@cam.ac.uk; jaa59@eng.cam.ac.uk; sh315@eng.cam.ac.uk).

Color versions of one or more figures in this article are available at <https://doi.org/10.1109/TTHZ.2022.3178875>.

Digital Object Identifier 10.1109/TTHZ.2022.3178875

range, broadly defined between 0.1 and 10 THz, has experienced an exceptionally fast growth in recent years, mostly driven by the great applications in strategic fields, such as spectroscopy, imaging, and communications [1]–[5]. The saturation of the available ranges in the RF and the increasing demand of applications striving for high data speeds, inevitably pushes the next generation of wireless communication beyond 5G toward the THz range. Approaches derived from electronics have reported an excellent performance lately in the lower part of the THz range, such as in CMOS integrated metasurface modulator operating at 300 GHz [6], but their efficiency sharply decreases at high frequencies. Thus, the need for an optoelectronic approach capable of being used over the whole THz range is reinforced and encouraged. Atmospheric attenuation sets the boundaries for the usage of THz band modulators to the mid- and near-field range and preferentially to frequencies lower than 1 THz, where resonant tunnelling diodes and uni-traveling-carrier photodiodes operate with sufficient power levels [7], [8]. The metamaterial (MM) approach, thanks to its versatility, efficiency, and miniaturization capabilities, is rapidly establishing itself as the privileged paradigm for the realization of integrated THz modulators [9]–[20]. Different strategies have been developed in order to include active materials in the MM designs, thus achieving a modulation. Amongst these, the most popular methodologies use phase-changing materials, such as VO<sub>2</sub>[21], [22], semiconductors [23], [24], liquid crystals [25], and 2-D materials, such as graphene [26], [27] and two-dimensional electron gases [28]–[31].

Graphene grants a wide carrier concentration modulation [32] and maintains high carrier mobilities at room temperature reported for industrially relevant chemical vapor deposition (CVD) techniques [33]. It can also be easily integrated into complex devices by using standard fabrication methods. The conductivity level can be modulated by acting on the Fermi energy optically, by chemical doping or electrostatic gating. Ion gel allows reaching Fermi energies  $>1$  eV, hence granting high-modulation depths, e.g., in [34]. However, such an approach is not consistent with the high reconfiguration speed required by some THz applications, mainly in THz wireless communications. The earliest active controlling of gated MMs/graphene devices were accomplished with a speed of modulation up to 10 kHz [26]. Several designs have been implemented after this pioneering work, such as MM/graphene in a hybrid resonators device was reported achieving  $\sim 40$  MHz of modulation speed

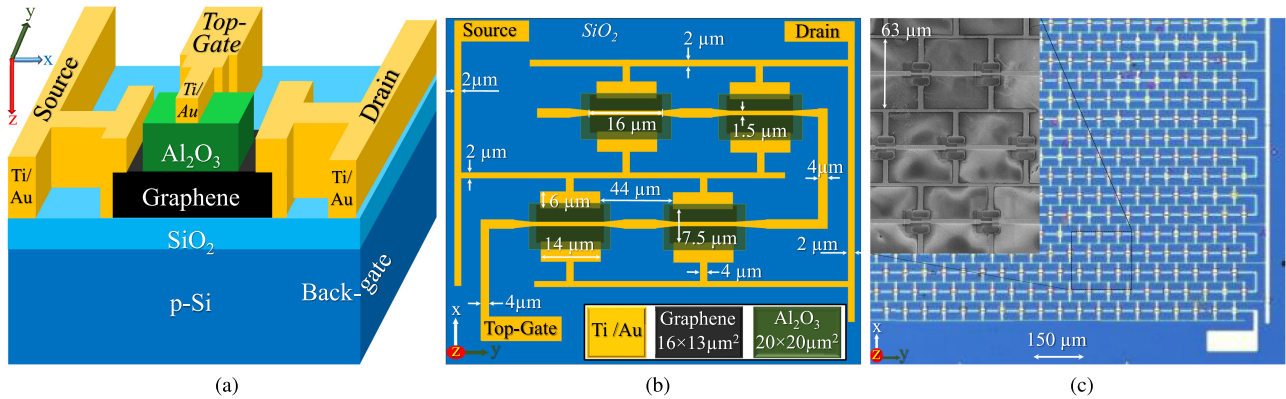


Fig. 1. Side-view (a) and top-view (b) of the device's structure and layers, and (c) optical microscope picture of a complete array of the fabricated Gated/SRs while the inset is the SEM image of a section of the SR array.

at a resonance of about 5 THz [35]. Metallic plasmonic antennas shunted by graphene patches reported a reconfiguration speed as high as  $\sim 115$  MHz [36]. Gated MM resonators shunted by graphene have been deployed to actively modulate the beam of THz light, i.e., amplitude, phase, and polarization, with the potential of achieving a high speed of modulation [37]–[40]. Recently, this approach has been used also with THz laser sources and for frequency combs stabilization [41], [42] due to its capability to control and alter the optical dispersion [43], [44].

In this work, we demonstrate how electrostatic gating can be implemented to achieve  $>3$  GHz reconfiguration speed with high efficiency of amplitude modulation depth ( $>7.6$  dB), significantly higher than the approximately 30% modification depth reported previously in [37] without modifying the graphene deposition techniques. This is achieved by using a double gate split-resonators (SRs) arrays with graphene patches shunting the device. Therefore, a preliminary theoretical optimization of the device was conducted by considering an electrical equivalent model together with a new design, which is based on the modulation of the interplay between meta-atoms collective response rather than addressing the single units. The device was simulated by adapting the lumped circuit model already described in [36] opportunely scaled to take into account the single-unit cell different geometry and nested arrangements, similar to the design reported in [30] and [31]. Graphene resistivity together with the internal capacitance between graphene to source and graphene to drain pads provide the ultimate RC constant limitations of the device's speed. This was reported to be in the order of a few GHz as in [30], and our results are consistent with these findings. The model predicts a 3 dB frequency in the order of tenths of GHz, critically depending on the parasitic capacitance. The limited equipment available hinders a direct verification of the simulated values and a feedback on the theoretical model as in [36]. Finally, to demonstrate the versatility of this device as an external modulator, a polarization modulation scheme has been set up using cross polarizers. In [37], the polarization modulation was achieved by using an electromagnetically induced transparency technique. Whereas in [38], the double layer of MM/graphene polarization device was fabricated to yield an artificial chiral response.

Here we basically exploit the strong amplitude and phase anisotropy of this new architecture to achieve an ellipticity

modulation of  $>40\%$  and a dynamic rotation of the polarization plane by  $>9^\circ$  at 0.68 THz and 0.75 THz frequencies, respectively. It is worth mentioning that these values have been calculated by using temporal resolved measurements and considering only the first transmitted pulse, thus neglecting Fabry Perot resonances at the sample's boundaries. By considering the entire transmitted time waveform, as in [45], the ellipticity change increases to  $\sim 60\%$  at 0.71 THz, while the rotation angle can be actively tuned more than  $20^\circ$  at 0.66 THz. Significantly, similar polarization modulation performances are achieved with GHz instead of MHz reconfiguration speed. This article is organized as follows. The first section is centered on the device's design and fabrication, the second one reports the experimental setup used for the data acquisition, and the third is a demonstration of the modulator's optoelectronic response in the THz range in different SR configurations. Finally, the experimental measurements and their critical evaluation are reported in Section III. The phase and amplitude transmission curves recorded at different gate voltages are compared with the simulations performed with finite-element method-based commercial software.

## II. FABRICATION AND EXPERIMENTAL SETUP

In order to maximize the modulation speed, a particular attention was devoted to a preliminary optimization of the design by using LTspice software, i.e., in reduction of capacitances, resistances, and footprint of the gated SRs [23], [31], [35], [46]. Our approach consists of designing MM/graphene devices fabricated on top of a commercially available  $\text{SiO}_2/\text{Si}$  (300 nm,  $500 \mu\text{m}$ ) substrate. The Si substrate is a slightly p-doped wafer, to allow back gating. Details on the modulator's structure are illustrated in Fig. 1(a). The total size of the array is  $1.3 \times 1.2 \text{ mm}^2$  and it comprises  $22 \times 20$  identical interdigitated SR units electrically connected in a nested arrangement. The fabrication process begins with a graphene monolayer grown via CVD and transferred on top of  $\text{SiO}_2/\text{Si}$  samples [47]. Next, the graphene layer is patterned into an array of rectangular features of  $16 \times 13 \mu\text{m}^2$  using optical lithography followed by  $\text{O}_2$  RF plasma ashing. The SRs are formed with a  $7.5 \mu\text{m}$  gap spacing. The SR features are patterned using a photolithography step followed by thermal evaporating Ti/Au (10 nm/150 nm) and lift off. The SRs along with the graphene patches are encapsulated by a 150 nm thick

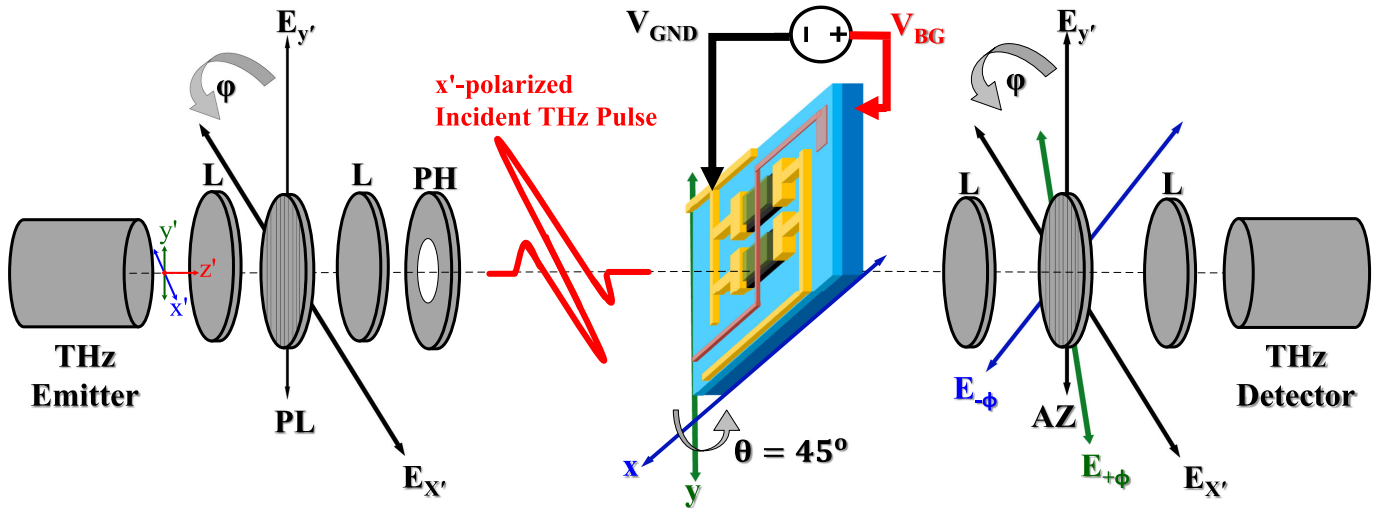


Fig. 2. Schematic of the THz time-domain spectroscopy (THz-TDS) experimental setup to acquire the temporal pulses of a THz source where  $\theta$  and  $\phi$  are rotational angles with respect to  $x'$  and  $y'$  respectively. L: Lenses, PL: Polarizer, PH: Pinhole (Iris),  $V_{\text{GND}}$ : Source/drain terminals,  $V_{\text{BG}}$ : Back or top gates terminals, and AZ: Analyzer.

$\text{Al}_2\text{O}_3$  layer deposited via atomic layer deposition in order to electrically isolate the SRs from the top gate. Additionally, the  $\text{Al}_2\text{O}_3$  layer minimizes graphene's hysteresis and the required Dirac point driving voltage when compared with an unprotected graphene patch [48]. The final step is the fabrication of the top gate features in correspondence with the SR's center, as shown in Fig. 1(a). The top gate feature is realized with electron beam lithography, Ti/Au thermal evaporation (10 nm/120 nm), and lift off. An optical microscope picture of a complete array is shown in Fig. 1(b), along with the scanning electron microscope (SEM) picture of the fabricated modulator in the inset of Fig. 1(b).

Experimental characterizations of the external THz modulator are conducted by using the THz time-domain spectroscopy (THz-TDS) system from Menlo Systems, model Tera K15, modified with two metallic grid polarizers to monitor the polarization status of the incoming and detected radiation. A schematic view of the THz-TDS setup is illustrated in Fig. 2. Electrical access to the device is achieved via several channels. The device is mounted onto a high speed-board with RF connections and wire-bonded. Source and drain pads are connected to the respective sides of the SR gaps shunted by graphene in the interdigitated scheme, as shown in Fig. 1(b). The top, back, and surface gates are connected to independent channels to allow full characterizations of the device. To actively bias the modulator, source-measure-units (SMUs) from the Keithley model 2450 are used to apply various voltages while monitoring the leakage current ( $I_{\text{BG}}$ ) toward the gate. The source and drain resonators pads are directly connected to the graphene patches, whose conductivity can be varied by acting on the gates.

### III. RESULTS AND DISCUSSION

#### A. Spectral Amplitude and Phase Modulations

In this work, the MM/graphene active devices are simulated using the RF module of COMSOL Multiphysics software. The electromagnetic response of a single MM unit is simulated, which under the periodic boundary conditions is representative

of the real array composed of hundreds of resonators. The software allows the retrieval of  $S_{11}$  and  $S_{21}$  complex parameters. A Drude model is used to simulate both the graphene and the Au conductivities following a model already reported elsewhere in [37]–[40]. The  $E_z$ -field concentrated in the capacitive gap is simulated for the graphene conductivities of 0.2 mS and 1.6 mS indicating the high and low modes at resonance, as shown by Fig. 3(a) and (b), respectively, whilst a 3-D plot of the unit cell showing the  $E_{\text{norm}}$ -field is reported in Fig. 3(c). The transmitted electric field is obtained by plotting the amplitude of  $S_{21}$  parameter. Fig. 3(d) reports a 7.8 dB difference in the simulated transmitted  $E$ -field amplitudes in the graphene conductivity ( $\sigma_{\text{Graphene}}$ ) range between 0.2 and 1.1 mS; which well reproduces the experimental data shown in Fig. 3(f), and it is consistent with the conductivity values already reported in [37]–[39]. The same  $\sigma_{\text{Graphene}}$  range is simulated as well to compare the transmitted spectral phase of the  $E$ -field polarized parallel to the SRs' gap, as shown in Fig. 3(e). Fig. 3(g) illustrates the measured experimental spectral phase difference of about  $17.4^\circ$  between bias backgate voltages ( $V_{\text{BG}}$ ) of  $-120$  V and  $+25$  V.

To study the modulation depth and relative phase changes of an incident THz  $E$ -field experimentally, the device is inserted in the THz-TDS setup shown in Fig. 2. Without the polarizer, the device's angle is set to  $\theta = 0^\circ$  while the analyzer is rotated by  $\phi = 90^\circ$  (full transmission). This corresponds with having the incoming  $E$ -field polarized parallel to the SRs' gaps, thus exciting the  $LC$  resonance. The modulator biasing configuration is electrically wired by connecting both the source and drain pads altogether to the ground ( $V_{\text{GND}}$ ), whereas the surface gate and backgate are connected to the SMU's positive terminal ( $V_{\text{BG}}$ ). After acquiring the transmitted THz data, the  $E$ -field is normalized to the calculated impinging spot size after the pinhole to a uniform  $1.2 \times 1.2 \text{ mm}^2$  area of graphene patch defined on the same chip without any metal features. This step is crucial to illuminate the effect of the THz radiation passing through the substrate and graphene layer. During postprocessing, only the first transmitted temporal pulse is considered [as shown in the

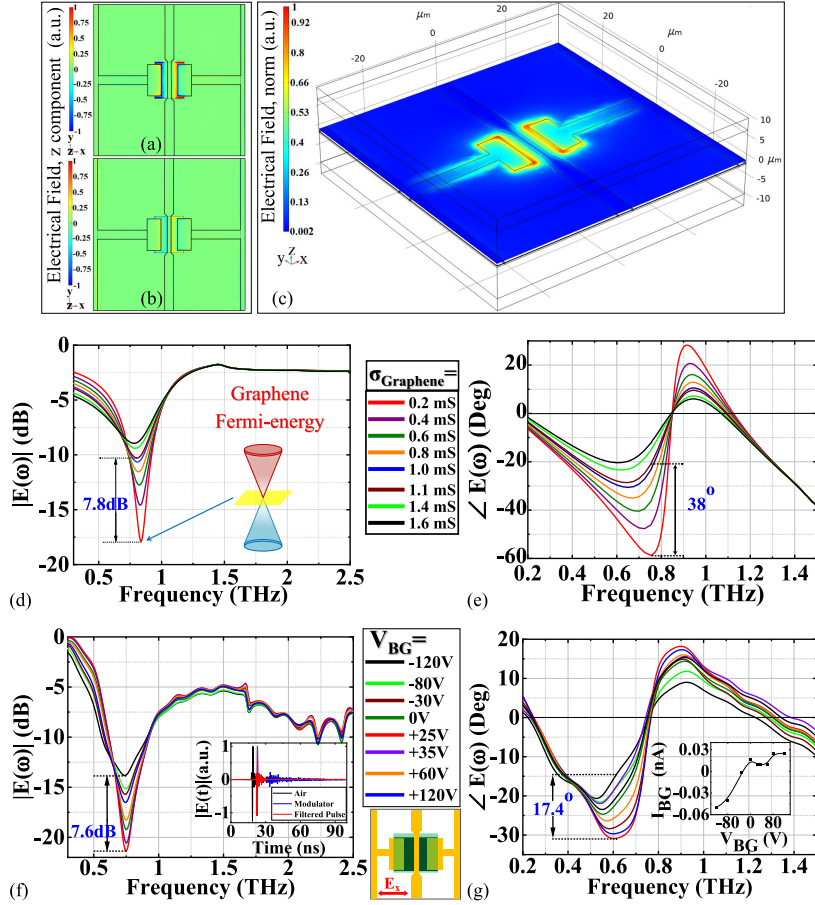


Fig. 3. Simulation of the transmitted  $E$ -field at  $\sigma_{\text{Graphene}} = 0.2 \text{ mS}$  (a) and  $1.6 \text{ mS}$  (b) at the resonant frequency of  $0.8 \text{ THz}$  calculated  $10 \text{ nm}$  above the source and drain gold layer. (c) 3-D simulated unit cell reporting the normalized  $E$ -field calculated with the same parameters used in (a) calculated  $500 \text{ nm}$  above the top-gate gold stripe. Spectral amplitude (d) and phase (e) were simulated for various graphene conductivities. THz-TDS experimental measurements of the transmitted  $E$ -field spectral amplitude (f) and phase (g) are shown for different  $V_{\text{BG}}$ . The inset of (f) is the acquired temporal pulses, while the inset of (g) is the leakage current toward backgate.

inset of Fig. 3(f)] by cropping the waveforms and zero-padding the rest of the time waveform to ease the postprocessing calculations and the overall discussion. By including in the calculations all the Fabry Perot reflections, however, the modulation efficiency increases being closer to the performance achievable with a cw laser source.

The modulator is biased with a range of  $V_{\text{BG}}$  between  $-120$  and  $+120 \text{ V}$ . The spectral amplitude attenuation with the different backgate biases is plotted in Fig. 3(f). More than  $7.6 \text{ dB}$  of extinction ratio between the Dirac point voltage (i.e.,  $V_{\text{BG}} = +25 \text{ V}$ ) and the  $V_{\text{BG}}$  of  $-120 \text{ V}$  is achievable. Additionally,  $>17.4^\circ$  in spectral relative phase change is feasible by driving the modulator between  $-120$  and  $+25 \text{ V}$ , as shown in Fig. 3(g). The leakage current ( $I_{\text{BG}}$ ) toward backgate is constantly monitored, reporting sub-nA values as shown by the inset of Fig. 3(g). By including all temporal pulses, the spectral amplitude, and phase modulations increase to  $>10 \text{ dB}$  at  $0.74 \text{ THz}$  and  $>27^\circ$  at  $0.62 \text{ THz}$ , respectively, when biasing the modulator between  $-120$  and  $+25 \text{ V}$ .

### B. Polarization Modulation

The same device can be implemented in a proof-of-principle experimental configuration to demonstrate its potential use as

a polarization modulator, highlighting either its optical activity (OA) or circular dichroism (CD) modulation performance. The physical mechanism here is based on the artificial birefringence which can be changed by tuning the graphene's Fermi energy, as in classical phase modulator schemes, e.g., as in [49]. However, standard electro-optic approach is impractical at these wavelengths, whilst here a dynamic modulation of the polarization state is achieved by using a submicron thick graphene loaded metasurface. The same approach can be expanded by implementing multiple layers of metasurface to enhance the optical response or different substrates, e.g., undoped Si, to reduce the transmission losses. It is worth stressing that the overall dynamic ranges recorded are comparable with similar designs as shown in [37] and [38] or alternative methods [50] but with  $>3 \text{ GHz}$  reconfiguration speed. To extract the THz radiation polarization state, the horizontally polarized  $E$ -field passing through a polarizer rotated by  $\phi = 90^\circ$  is incident on the device rotated by  $\theta = 45^\circ$ . The emergent  $E$ -field is passing through an analyzer with the selected angles of  $\phi = \pm 45^\circ$ . Similar to the THz antenna emitter, the detector is positioned at the horizontal polarization state.

When rotating the SRs by  $\theta = 45^\circ$ , the horizontally polarized incident  $E$ -field wave is divided into two components. Hence, the two linear transmission  $E$ -fields (i.e.,  $E_{\pm 45^\circ}$ ) are required to

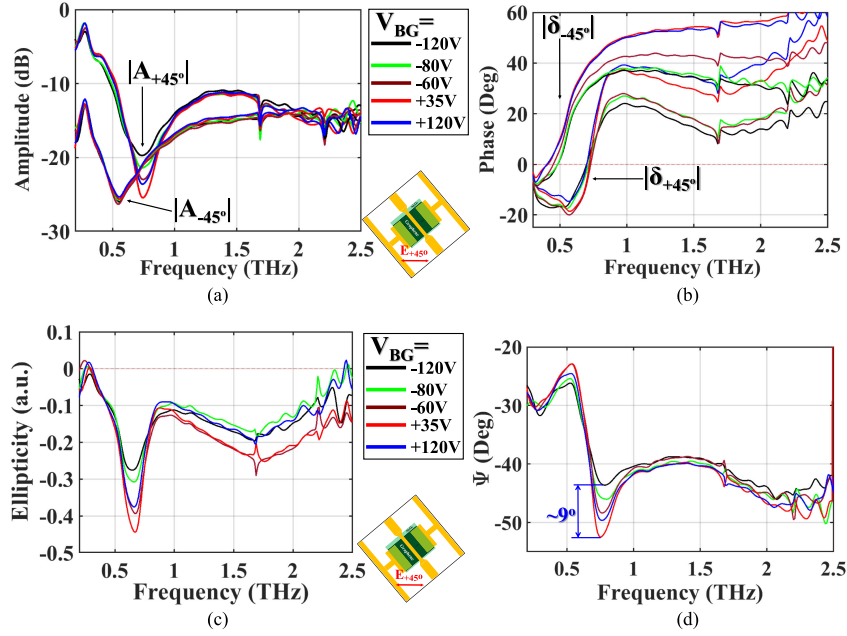


Fig. 4. Linear transmission of the  $E$ -field spectral amplitude (a) and relative phase (b), and ellipticity (c) and rotational angle (d) at various  $V_{BG}$ .

retrieve the right and left circular polarization (RCP and LCP) amplitudes ( $|A_{\pm 45^\circ}|$ ) and phases ( $\delta_{\pm 45^\circ}$ ) as follows [51]:

$$\begin{aligned} \begin{pmatrix} E_{RCP} \\ E_{LCP} \end{pmatrix} &= \frac{1}{\sqrt{2}} \begin{pmatrix} 1 & i \\ 1 & -i \end{pmatrix} \begin{pmatrix} E_{+45^\circ} \\ E_{-45^\circ} \end{pmatrix} \\ &= \frac{1}{\sqrt{2}} \begin{pmatrix} 1 & i \\ 1 & -i \end{pmatrix} \begin{pmatrix} |A_{+45^\circ}| e^{i\delta_{+45^\circ}} \\ |A_{-45^\circ}| e^{i\delta_{-45^\circ}} \end{pmatrix} \end{aligned} \quad (1)$$

where the  $E_{RCP}$  and  $E_{LCP}$  are the transmitted right and left circularly polarized components, respectively [51]. The  $E_{\pm 45^\circ}$  amplitudes and phases are selected by the analyzer and normalized with respect to the square graphene patch rotated by  $45^\circ$ . Since both incoming  $E_{x,y}$  are excited simultaneously, the transmitted components along  $x$  and  $y$  are selected by changing the analyzer angle ( $\phi$ ). These latter curves are plotted in Fig. 4(a) and (b). In both experiments,  $V_{BG}$  is swept from  $-120$  to  $+120$  V. The complex values of the transmitted  $E$ -fields are used to calculate the polarization ellipticity ( $\eta$ ) and rotational angle ( $\Psi$ ) which quantify CD and OA, respectively, and to retrieve the state of polarization ellipses as follows [25], [51]–[53]:

$$\eta = \frac{|E_{RCP}| - |E_{LCP}|}{|E_{RCP}| + |E_{LCP}|} \quad (2)$$

$$\psi = \frac{1}{2} \tan^{-1} \{ \tan(2\epsilon) \cos(\Delta\delta) \} \quad (3)$$

$$\frac{E_x^2}{|A_{+45^\circ}|^2} - \frac{2E_x E_y \cos \Delta\delta}{|A_{+45^\circ}| |A_{-45^\circ}|} + \frac{E_y^2}{|A_{-45^\circ}|^2} = \sin^2 \Delta\delta \quad (4)$$

where  $\epsilon = |A_{+45^\circ}| / |A_{-45^\circ}|$  and  $\Delta\delta = \delta_{+45^\circ} - \delta_{-45^\circ}$  are both inserted in (3) and (4).  $E_{RCP}$  and  $E_{LCP}$  are extracted via (1). After solving the quadratic equation (4) using the polar coordinates, the magnitudes are normalized with respect to their maximum values.

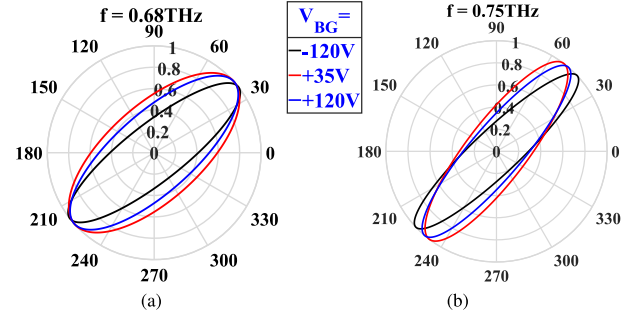


Fig. 5. Polarization ellipses for (a) 0.68 THz, and (b) 0.75 THz.

By acting on the backgate, the graphene conductivity range is swept, thus changing the transmitted  $E$ -field amplitudes and phases of the device's symmetry axis. At a frequency of 0.68 THz, the maximum modulation of ellipticity from  $-0.27$  to  $-0.44$  is recorded when biasing the modulator from  $-120$  to  $+35$  V, as presented by Fig. 4(c). The modulated ellipses with  $\sim 40\%$  changes in ellipticity are illustrated in Fig. 5(a). The Dirac point in this device is found between  $+25$  V (the first amplitude measurements in Section III-A) and  $+35$  V (in the polarization measurements acquired months afterward). The change in ellipticity is accompanied by a minimal change in the OA around  $45^\circ$ , as shown in Fig. 4(d). This range of frequencies is consistent with the largest phase accumulation as plotted in Fig. 4(b). At a frequency of 0.75 THz, the ellipticity has minimal changes from  $-0.2$  to  $-0.27$  for several backgate biases from  $-120$  to  $+35$  V, respectively. At the same time, the polarization angle is rotated notably by  $9^\circ$ , as illustrated by Fig. 4(d) and the ellipses in Fig. 5(b). Around this frequency region, the depth of spectral amplitude modulation is reaching its maximum value near to the SRs' resonance, as shown in Fig. 4(a). The inclusion of multiple Fabry Perot resonances yields for  $\Psi$  and

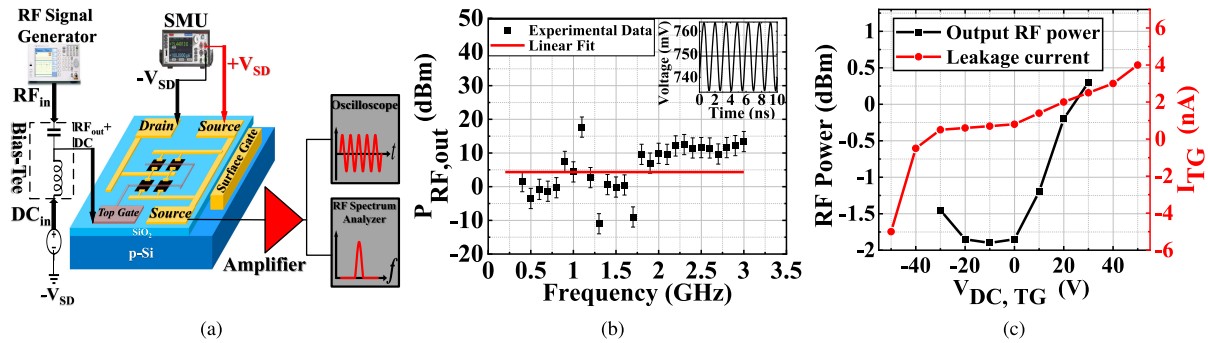


Fig. 6. (a) Schematic of the RF electrical setup, (b) frequency response of the modulator (inset is the 700 MHz output waveform), and (c) output RF power for 750 MHz frequency and leakage current towards top gate for different dc biases.

$\eta$  modulations increase to  $>20^\circ$  at 0.66 THz and  $>60\%$  at 0.71 THz, respectively, when biasing the modulator between  $-120$  to  $+35$  V.

#### IV. RF ELECTRICAL CHARACTERIZATION

In a separate set of experiments, the device is finally mounted on a high-speed circuit board in order to investigate its reconfiguration speed. For practical applications, the device is driven by using the top-gate, instead of the back-gate, to allow for lower biases and for more robustness with respect to shortage and leakage currents. Hence, a wider voltage range is accessible for characterisations. An RF signal, generated with an Agilent RF generator model N9310 A, is mixed with a dc voltage ( $V_{DC}$ ) thanks to a bias-tee (model ZX85-12G-S+ from Mini-Circuits). The importance of the applied dc voltage is to offset the input RF signal along the curve of Dirac point voltage. The  $RF_{out}+dc$  signal is applied between the top gate and drain pads to modulate the graphene conductivity. The drain pad acts as a common ground throughout these measurements. The source ( $+V_{SD}$ ) and drain ( $-V_{SD}$ ) pads are connected separately to an SMU providing a fixed current of 700 nA. The modulated voltage between the source and drain pads is detected and fed to an external low noise amplifier, model ZX60-83LN-S+ from Mini-Circuits, to boost its amplitude. The output RF signal is monitored by an oscilloscope and an RF spectrum analyzer from Rohde & Schwarz, model FS300. The RF electrical characterization setup is illustrated in Fig. 6(a).

When driving the modulator with an input RF power of  $+20$  dBm and an offset dc voltage ( $V_{DC}$ ) of  $+20$  V, the modulator shows a well-established response to all frequencies up to 3 GHz as plotted in Fig. 6(b). It should be noted that the output RF power fluctuations at different frequencies are due to impedance mismatch, and the speed limitations are subject to instruments availability. The output waveform for a frequency of 700 MHz is plotted as an inset in Fig. 6(b) showing a dc voltage offset of  $\sim 750$  mV, which corresponds to the potential voltage between the source and drain pads. Fig. 6(c) reports the modulator's response at a fixed frequency of 750 MHz for different input  $V_{DC}$  biases. The output RF power is decreasing as  $V_{DC,TG}$  increases till reaching its minimum around the Dirac voltage,  $\sim 10$  V, providing a good agreement with the results reported previously in the Sections III-A and III-B and illustrated in Fig. 6(c). The

output RF power attenuation with different input driving dc voltages is to be ascribed to the change of graphene conductivity. The Dirac voltage is found around  $+10$  V with 150 nm thickness of  $Al_2O_3$  gate dielectric which is consistent with the 25–30 V voltages required to reach Dirac point with the backgate where the  $SiO_2$  dielectric thickness is 300 nm.

Notice that the leakage current toward top gate ( $I_{TG}$ ) is  $\sim 100$  times smaller than the  $I_{SD}$ , as shown in Fig. 6(c). It is important to mention that the RF signal generator, bias-tee, external amplifier, oscilloscope, and RF spectrum analyzer are only limited to a few GHz. This device could operate up to tenths of GHz according to our model, and therefore, a different approach should be envisaged either all optically or with a high-frequency vector network analyzers.

#### V. CONCLUSION

In this work, we present an efficient and ultrafast modulator operating in the THz range based on an MM array loaded with graphene. A maximum amplitude modulation depth of  $>80\%$  and phase modulation of  $>17^\circ$  were reported around the resonant frequency of 0.8 THz. In a further set of experiments aiming to exploit the versatility of this active metasurface, the CD and OA were investigated recording  $>40\%$  in ellipticity modulation at 0.68 THz and a rotation angle tunability of  $>9^\circ$ . When considering all temporal pulses, the depth of amplitude and phase modulations increase to  $>90\%$  and  $>27^\circ$ , respectively. Additionally, the ellipticity and rotational angle changes exceed 60% and  $20^\circ$ , respectively. Finally, the high performance of the device was achieved without affecting the measured reconfiguration speed, which was reported to reach at least 3 GHz, limited only by the available instrumentation. This represents a progress of 10 times higher reconfiguration speed compared with previous similar all-electronic THz devices integrating graphene as a functional material. These results represent a breakthrough for many applications where fast and efficient THz circuitry is required, such as THz wireless communication or quantum electronics for active modelocking of QCLs.

#### ACKNOWLEDGMENT

Datasets that support the findings of this study are openly available from Lancaster University's repository PURE at <https://doi.org/10.17635/lancaster/researchdata/526>.

## REFERENCES

- [1] T. Nagatsuma, G. Ducournau, and C. C. Renaud, "Advances in terahertz communications accelerated by photonics," *Nature Photon.*, vol. 10, no. 6, pp. 371–379, May 2016.
- [2] H. Elayan, O. Amin, B. Shihada, R. M. Shubair, and M.-S. Alouini, "Terahertz band: The last piece of RF spectrum puzzle for communication systems," *IEEE Open J. Commun. Soc.*, vol. 1, pp. 1–32, Nov. 2020.
- [3] L. Zhang, X. Pang, S. Jia, S. Wang, and X. Yu, "Beyond 100 Gb/s optoelectronic terahertz communications: Key technologies and directions," *IEEE Commun. Mag.*, vol. 58, no. 11, pp. 34–40, Nov. 2020.
- [4] F. Fan *et al.*, "Magnetically induced terahertz birefringence and chirality manipulation in transverse-magnetized metasurface," *Adv. Opt. Mater.*, vol. 9, no. 24, Sep. 2021, Art. no. 2101097.
- [5] H. Zeng *et al.*, "High-precision digital terahertz phase manipulation within a multichannel field perturbation coding chip," *Nature Photon.*, vol. 15, no. 10, pp. 751–757, Aug. 2021.
- [6] S. Venkatesh, X. Lu, H. Saeidi, and K. Sengupta, "A high-speed programmable and scalable terahertz holographic metasurface based on tiled CMOS chips," *Nature Electron.*, vol. 3, no. 12, pp. 785–793, Dec. 2020.
- [7] C. Lin and G. Y. L. Li, "Terahertz communications: An array-of-subarrays solution," *IEEE Commun. Mag.*, vol. 54, no. 12, pp. 124–131, Dec. 2016.
- [8] T. Kürner, D. Mittleman, and T. Nagatsuma, *THz Communications: Paving the Way Towards Wireless Tbps*. Berlin, Germany: Springer, 2021.
- [9] T. Low and P. Avouris, "Graphene plasmonics for terahertz to mid-infrared applications," *ACS Nano*, vol. 8, no. 2, pp. 1086–1101, Jan. 2014.
- [10] H.-T. Chen, A. J. Taylor, and N. Yu, "A review of metasurfaces: Physics and applications," *Rep. Prog. Phys.*, vol. 79, no. 7, Jun. 2016, Art. no. 076401.
- [11] Z. Wang, F. Cheng, T. Winsor, and Y. Liu, "Optical chiral metamaterials: A review of the fundamentals, fabrication methods and applications," *Nanotechnology*, vol. 27, no. 41, Sep. 2016, Art. no. 412001.
- [12] I. Al-Naib and W. Withayachumnanukul, "Recent progress in terahertz metasurfaces," *J. Infrared Milli Terahz Waves*, vol. 38, no. 9, pp. 1067–1084, Mar. 2017.
- [13] Z. Ma, Z. Geng, Z. Fan, J. Liu, and H. Chen, "Modulators for terahertz communication: The current state of the art," *Research*, vol. 2019, May 2019, Art. no. 6482975.
- [14] R. Degl'Innocenti, S. J. Kindness, H. E. Beere, and D. A. Ritchie, "All-integrated terahertz modulators," *Nanophotonics*, vol. 7, no. 1, pp. 127–144, Oct. 2018.
- [15] S. Yoo and Q.-H. Park, "Metamaterials and chiral sensing: A review of fundamentals and applications," *Nanophotonics*, vol. 8, no. 2, pp. 249–261, Jan. 2019.
- [16] J. Li *et al.*, "Metal-graphene hybrid active chiral metasurfaces for dynamic terahertz wavefront modulation and near field imaging," *Carbon*, vol. 163, pp. 34–42, Aug. 2020.
- [17] S. Lee *et al.*, "Metamaterials for enhanced optical responses and their application to active control of terahertz waves," *Adv. Mater.*, vol. 32, no. 35, Mar. 2020, Art. no. 2000250.
- [18] Z. Yaxin *et al.*, "Terahertz smart dynamic and active functional electromagnetic metasurfaces and their applications," *Phil. Trans. R. Soc. A.*, vol. 378, no. 2182, Sep. 2020, Art. no. 20190609.
- [19] X. Fu, F. Yang, C. Liu, X. Wu, and T. J. Cui, "Terahertz beam steering technologies: From phased arrays to field-programmable metasurfaces," *Adv. Opt. Mater.*, vol. 8, no. 3, 2020, Art. no. 1900628.
- [20] S. Shen *et al.*, "Recent advances in the development of materials for terahertz metamaterial sensing," *Adv. Opt. Mater.*, vol. 10, no. 1, 2022, Art. no. 2101008.
- [21] M. A. Kats *et al.*, "Thermal tuning of mid-infrared plasmonic antenna arrays using a phase change material," *Opt. Lett.*, vol. 38, no. 3, pp. 368–370, Feb. 2013.
- [22] A. V. Ivanov *et al.*, "Fabrication of epitaxial W-doped VO<sub>2</sub> nanostructured films for terahertz modulation using the solvothermal process," *ACS Appl. Nano Mater.*, vol. 4, no. 10, pp. 10592–10600, Oct. 2021.
- [23] H.-T. Chen *et al.*, "Active terahertz metamaterial devices," *Nature*, vol. 444, no. 7119, pp. 597–600, Nov. 2006.
- [24] P. Pitchappa *et al.*, "Chalcogenide phase change material for active terahertz photonics," *Adv. Mater.*, vol. 31, no. 12, 2019, Art. no. 1808157.
- [25] Y. Ji, F. Fan, S. Xu, J. Yu, and S. Chang, "Manipulation enhancement of terahertz liquid crystal phase shifter magnetically induced by ferromagnetic nanoparticles," *Nanoscale*, vol. 11, no. 11, pp. 4933–4941, Feb. 2019.
- [26] S. H. Lee *et al.*, "Switching terahertz waves with gate-controlled active graphene metamaterials," *Nature Mater.*, vol. 11, no. 11, pp. 936–941, Sep. 2012.
- [27] Q. Zheng, L. Xia, L. Tang, C. Du, and H. Cui, "Low voltage graphene-based amplitude modulator for high efficiency terahertz modulation," *Nanomaterials*, vol. 10, no. 3, Mar. 2020. [Online]. Available; <https://www.mdpi.com/2079-4991/10/3/585>
- [28] P. Singh and S. Sonkusale, "High speed terahertz modulator on the chip based on tunable terahertz slot waveguide," *Sci. Rep.*, vol. 7, no. 1, pp. 1–8, Jan. 2017.
- [29] T. Kleine-Ostmann, P. Dawson, K. Pierz, G. Hein, and M. Koch, "Room-temperature operation of an electrically driven terahertz modulator," *Appl. Phys. Lett.*, vol. 84, no. 18, pp. 3555–3557, Apr. 2004.
- [30] Y. Zhang *et al.*, "Gbps terahertz external modulator based on a composite metamaterial with a double-channel heterostructure," *Nano Lett.*, vol. 15, no. 5, pp. 3501–3506, Apr. 2015.
- [31] Y. Zhao *et al.*, "High-speed efficient terahertz modulation based on tunable collective-individual state conversion within an active 3 nm two-dimensional electron gas metasurface," *Nano Lett.*, vol. 19, no. 11, pp. 7588–7597, Aug. 2019.
- [32] D. K. Efetov and P. Kim, "Controlling electron-phonon interactions in graphene at ultrahigh carrier densities," *Phys. Rev. Lett.*, vol. 105, Dec. 2010, Art. no. 256805.
- [33] D. De Fazio *et al.*, "High-mobility, wet-transferred graphene grown by chemical vapor deposition," *ACS Nano*, vol. 13, no. 8, pp. 8926–8935, Jul. 2019.
- [34] Y. Malevich, M. S. Ergoktas, G. Bakan, P. Steiner, and C. Kocabas, "Video-speed graphene modulator arrays for terahertz imaging applications," *ACS Photon.*, vol. 7, no. 9, pp. 2374–2380, Aug. 2020.
- [35] P. Q. Liu *et al.*, "Highly tunable hybrid metamaterials employing splitting resonators strongly coupled to graphene surface plasmons," *Nature Commun.*, vol. 6, no. 1, pp. 1–7, Nov. 2015.
- [36] D. S. Jessop *et al.*, "Graphene based plasmonic terahertz amplitude modulator operating above 100 MHz," *Appl. Phys. Lett.*, vol. 108, no. 17, Apr. 2016, Art. no. 171101.
- [37] S. J. Kindness *et al.*, "Graphene-integrated metamaterial device for all-electrical polarization control of terahertz quantum cascade lasers," *ACS Photon.*, vol. 6, no. 6, pp. 1547–1555, May 2019.
- [38] S. J. Kindness *et al.*, "A terahertz chiral metamaterial modulator," *Adv. Opt. Mater.*, vol. 8, no. 21, Aug. 2020, Art. no. 2000581.
- [39] S. J. Kindness *et al.*, "Active control of electromagnetically induced transparency in a terahertz metamaterial array with graphene for continuous resonance frequency tuning," *Adv. Opt. Mater.*, vol. 6, no. 21, Aug. 2018, Art. no. 1800570.
- [40] R. Degl'Innocenti *et al.*, "Fast room-temperature detection of terahertz quantum cascade lasers with graphene-loaded bow-tie plasmonic antenna arrays," *ACS Photon.*, vol. 3, no. 10, pp. 1747–1753, 2016.
- [41] D. Burghoff *et al.*, "Terahertz laser frequency combs," *Nature Photon.*, vol. 8, no. 6, pp. 462–467, May 2014.
- [42] M. Rösch, G. Scalari, M. Beck, and J. Faist, "Octave-spanning semiconductor laser," *Nature Photon.*, vol. 9, no. 1, pp. 42–47, Nov. 2015.
- [43] F. Wang *et al.*, "Short terahertz pulse generation from a dispersion compensated modelocked semiconductor laser," *Laser Photon. Rev.*, vol. 11, no. 4, Jul. 2017, Art. no. 1700013.
- [44] F. P. Mezzapesa *et al.*, "Tunable and compact dispersion compensation of broadband THz quantum cascade laser frequency combs," *Opt. Exp.*, vol. 27, no. 15, pp. 20231–20240, Jul. 2019.
- [45] S. J. Kindness *et al.*, "Active metamaterial polarization modulators for the terahertz frequency range," *J. Phys.: Conf. Ser.*, vol. 1571, no. 1, Jul. 2020, Art. no. 012003.
- [46] M. T. Nouman *et al.*, "Terahertz modulator based on metamaterials integrated with metal-semiconductor-metal varactors," *Sci. Rep.*, vol. 6, no. 1, pp. 1–7, May 2016.
- [47] O. J. Burton *et al.*, "The role and control of residual bulk oxygen in the catalytic growth of 2D materials," *J. Phys. Chem. C*, vol. 123, no. 26, pp. 16257–16267, Jun. 2019.
- [48] J. A. Alexander-Webber *et al.*, "Encapsulation of graphene transistors and vertical device integration by interface engineering with atomic layer deposited oxide," *2D Mater.*, vol. 4, no. 1, Dec. 2016, Art. no. 011008.
- [49] A. Yariv, *Quantum Electronics*, 3rd ed. New York, NY, USA: Wiley, 1989.
- [50] R. Degl'Innocenti, H. Lin, and M. Navarro-Cía, "Recent progress in terahertz metamaterial modulators," *Nanophotonics*, vol. 11, no. 8, pp. 1485–1514, Apr. 2022.
- [51] Y. Ji *et al.*, "Active terahertz spin state and optical chirality in liquid crystal chiral metasurface," *Phys. Rev. Mater.*, vol. 5, Aug. 2021, Art. no. 085201.
- [52] R. Lin *et al.*, "Multiple interference theoretical model for graphene metamaterial-based tunable broadband terahertz linear polarization converter design and optimization," *Opt. Exp.*, vol. 29, no. 19, pp. 30357–30370, Sep. 2021.
- [53] S. Wang, L. Kang, and D. H. Werner, "Active terahertz chiral metamaterials based on phase transition of vanadium dioxide (VO<sub>2</sub>)," *Sci. Rep.*, vol. 8, no. 1, pp. 1–9, Jan. 2018.